A Lagrangian dynamic subgrid-scale model of turbulence

By C. Meneveau[1], T. S. Lund[2] AND W. Cabot[2]

A new formulation of the dynamic subgrid-scale model is tested in which the error associated with the Germano identity is minimized over flow pathlines rather than over directions of statistical homogeneity. This procedure allows the application of the dynamic model *with averaging* to flows in complex geometries that do not possess homogeneous directions. The characteristic Lagrangian time scale over which the averaging is performed is chosen such that the model is purely dissipative, guaranteeing numerical stability when coupled with the Smagorinsky model. The formulation is tested successfully in forced and decaying isotropic turbulence and in fully developed and transitional channel flow. In homogeneous flows, the results are similar to those of the volume-averaged dynamic model, while in channel flow, the predictions are superior to those of the plane-averaged dynamic model. The relationship between the averaged terms in the model and vortical structures (worms) that appear in the LES is investigated. Computational overhead is kept small (about 10 % above the CPU requirements of the volume or plane-averaged dynamic model) by using an approximate scheme to advance the Lagrangian tracking through first-order Euler time integration and linear interpolation in space.

1. Introduction

The dynamic model (Germano *et al.*, 1991) for the parametrization of subgrid stresses in a Large-Eddy-Simulation (LES) is a means of utilizing information from the resolved turbulent velocity field $\tilde{u}_i(\mathbf{x},t)$ to dynamically compute model coefficients. It is based on the algebraic identity,

$$L_{ij} = T_{ij} - \overline{\tau}_{ij}, \tag{1}$$

where

$$L_{ij} = \overline{\tilde{u}_i\tilde{u}_j} - \overline{\tilde{u}}_i\overline{\tilde{u}}_i, \qquad T_{ij} = \widetilde{\tilde{u}_i\tilde{u}_j} - \overline{\tilde{u}}_i\overline{\tilde{u}}_j, \quad \text{and} \quad \tau_{ij} = \widetilde{u_iu_j} - \tilde{u}_i\tilde{u}_j. \tag{2}$$

Above, a *tilde* represents low-pass filtering with a filter-width of size Δ (comparable to the grid-size of the LES), while an *overbar* represents filtering at a scale 2Δ. When the identity is written with the stresses T_{ij} and τ_{ij} replaced by the Smagorinsky model, and Eq. (1) is enforced in a least-square error sense over all five independent

1 The Johns Hopkins University
2 Center for Turbulence Research

tensor elements (Lilly, 92), one obtains the following expression for the (dynamic) Smagorinsky coefficient:

$$c_s^2(\mathbf{x},t) = \frac{L_{pq}M_{pq}}{M_{pq}M_{pq}}, \tag{3}$$

where

$$M_{ij} = -2\Delta^2 \left[4|\overline{\tilde{S}}|\overline{\tilde{S}_{ij}} - \overline{|\tilde{S}|\tilde{S}_{ij}} \right], \tag{4}$$

and $\tilde{S}_{ij}$ is the resolved rate-of-strain tensor. This version of the dynamic model in which the coefficient can vary from point to point is often referred to as the 'local dynamic model'.

There are two problems associated with the local dynamic model (Eq. (3)). First, as pointed out by Ghosal *et al.* (1994), it is mathematically inconsistent to remove the coefficient from the filter operation (in $\overline{\tau_{ij}}$) as if it were a constant. Second, as observed during LES, during *a-priori* analysis of DNS data (Lund *et al.*, 1993) and when analyzing experimental data at high Reynolds numbers (Liu *et al.*, 1994; O'Neil & Meneveau, 1994), the coefficient field predicted by the local model varies strongly in space and contains a significant fraction of negative values. Negative values of c_s^2 are of particular concern because they lead to negative values of eddy viscosity in the Smagorinsky parameterization. This is destabilizing in a numerical simulation, and non-physical growth in the resolved velocity fluctuations is often observed (Lund *et al.*, 1993).

Historically, the first problem was given very little attention while the second problem was dealt with by averaging terms in the equations for c_s^2 over space and/or time. When averaged, the numerator in Eq. (3) was generally found to be positive, thus recovering the statistical notion of energy transfer to the subgrid scales. Averaging over homogeneous directions has been a popular choice, and excellent results were obtained in a variety of flows. As examples, Germano *et al.* (1991) and Piomelli (1993) average the equations over planes parallel to the walls in channel flow simulations whereas Akselvoll and Moin (1993) average over the spanwise direction in a backward-facing step flow. While these averaging schemes proved to be effective at controlling possible instabilities and led to accurate results, rigorous justification for them was lacking. Additionally, homogeneity in either space or time was required.

These problems as well as the lingering issue of extracting c_s^2 from the filtering operation were addressed by Ghosal *et al.* (1994) where a variational approach was used to account properly for the spatial variation of the coefficient within the filter operation. Using this approach, various prior models employing averaging were rigorously derived by imposing appropriate constraints in the solution to the variational problem. Finally, two stable local models were derived that did not make use of homogeneous directions. The first simply imposes the constraint that c_s^2 be non-negative. The second allows negative c_s^2 but enforces a budget for the reversed energy transfer through inclusion of a subgrid-scale kinetic energy equation. These latter two models have been tested in a variety of flows and are applicable to complex geometry flows under unsteady conditions.

While the work of Ghosal *et al.* (1994) has provided rigorously-derived methods applicable to inhomogeneous flows, there is still room for improvement. The constraint $c_s^2 \geq 0$ is hard to justify on other than heuristic grounds, and the numerical solution of the integral equation can be expensive. The kinetic energy formulation removes the conceptual problem associated with the constraint $c_s^2 \geq 0$, but only at the additional expense of two more integral equations and one transport equation. Also, new constraints for model coefficients in the kinetic energy equation have to be introduced. Therefore, schemes that make use of averaging continue to have appeal due to their demonstrated accuracy and relative ease of implementation. At the same time, current averaging schemes require at least one homogeneous direction (in space or time) and are therefore not applicable in fully inhomogeneous unsteady flows. If this restriction could be removed, an equally general and perhaps simpler alternative to the integral equation of Ghosal *et al.* (1994) would be available for inhomogeneous flow simulations.

The objective of this work is to develop a simple, but generally applicable, averaging scheme. As originally suggested by O'Neil & Meneveau (1993), we propose to average over particle trajectories rather than directions of statistical homogeneity. Particle trajectories are always well defined objects that in no way rely on special boundary conditions or assumptions of statistical homogeneity. Since particle trajectories are the natural directions associated with fluid flow, averaging the equations for c_s^2 over these directions has some physical appeal. It is reasonable to expect that turbulent eddies evolve along particle paths and that the turbulence energy cascade should be most apparent when viewed in a Lagrangian coordinate system. As reported by Meneveau & Lund (1994), there is evidence to suggest that this is indeed the case. If the energy cascade does in fact proceed mainly along fluid trajectories, then it would seem logical to postulate that the subgrid-scale model coefficient at a given point $\mathbf{x}$ should depend in some way on the history of the flow along the trajectory leading to $\mathbf{x}$. This picture should be contrasted with that of conventional schemes where spatial averaging removes the local details of the flow structure and the turbulence development history is completely ignored. Eulerian time averaging suffers from similar deficiencies since the advection of structures is ignored.

The Lagrangian model is derived by requiring that the error in Germano's identity be minimized along fluid trajectories. This procedure leads to a pair of relaxation transport equations that carry the statistics forward in Lagrangian time. We show that these equations can be solved in an approximate fashion in a numerically efficient way. The model is applied to a variety of test cases including forced and decaying isotropic turbulence, fully developed channel flow, and transitional channel flow. In each case, the model is shown to produce results equal or superior to those of spatially-averaged versions of the dynamic model. At the same time, the numerical solutions to the transport equations increase the computational workload by only about 10% as compared with the spatially-averaged approach.

2. The Lagrangian dynamic model

2.1 Formulation

We propose to determine the model coefficient $c_s^2(\mathbf{x},t)$ by minimizing the error in Germano's identity along particle trajectories. Consider a particle located at position $\mathbf{x}$ at time t. The trajectory of this particle for earlier times $t' < t$ is

$$\mathbf{z}(t) = \mathbf{x} - \int_{t'}^{t} \tilde{\mathbf{u}}[z(t''),t'']dt'' \tag{5}$$

The error associated with Germano's identity at any point along the trajectory is

$$e_{ij}(\mathbf{z},t') = c_s^2(\mathbf{z},t')M_{ij}(\mathbf{z},t') - L_{ij}(\mathbf{z},t'). \tag{6}$$

Here we have assumed that c_s^2 varies negligibly in space over the scale of the test filter and have therefore removed it from the filter operation.

The total error is defined as the pathline accumulation of the local error squared,

$$E = \int_{-\infty}^{t} e_{ij}(\mathbf{z}(t'),t')\, e_{ij}(\mathbf{z}(t'),t')\, W(t-t')\, dt' \tag{7}$$

The weighting function $W(t-t')$ is introduced here in order to control the relative importance of events near time t with those of earlier times. As described below, we shall weight the error at time t most strongly and assign a decreasing weight to earlier times. It is now assumed that c_s^2 varies negligibly in time over the scale of the weighting function $W(t-t')$. In this case, $c_s^2(\mathbf{z},t')$ may be replaced by $c_s^2(\mathbf{x},t)$, and the total error is then minimized with respect to c_s^2 by enforcing

$$\frac{\partial E}{\partial c_s^2} = \int_{-\infty}^{t} 2e_{ij}\frac{\partial e_{ij}}{\partial c_s^2}\, W(t-t')\, dt' = 0. \tag{8}$$

Making use of Eq. (6) (with $c_s^2(\mathbf{z},t')$ replaced by $c_s^2(\mathbf{x},t)$) and solving for c_s^2, one then obtains

$$c_s^2(\mathbf{x},t) = \frac{\mathcal{I}_{LM}}{\mathcal{I}_{MM}}, \tag{9}$$

where

$$\mathcal{I}_{LM}(\mathbf{x},t) = \int_{-\infty}^{t} L_{ij}M_{ij}(\mathbf{z}(t'),t')\, W(t-t')\, dt', \tag{10}$$

$$\mathcal{I}_{MM}(\mathbf{x},t) = \int_{-\infty}^{t} M_{ij}M_{ij}(\mathbf{z}(t'),t')\, W(t-t')\, dt', \tag{11}$$

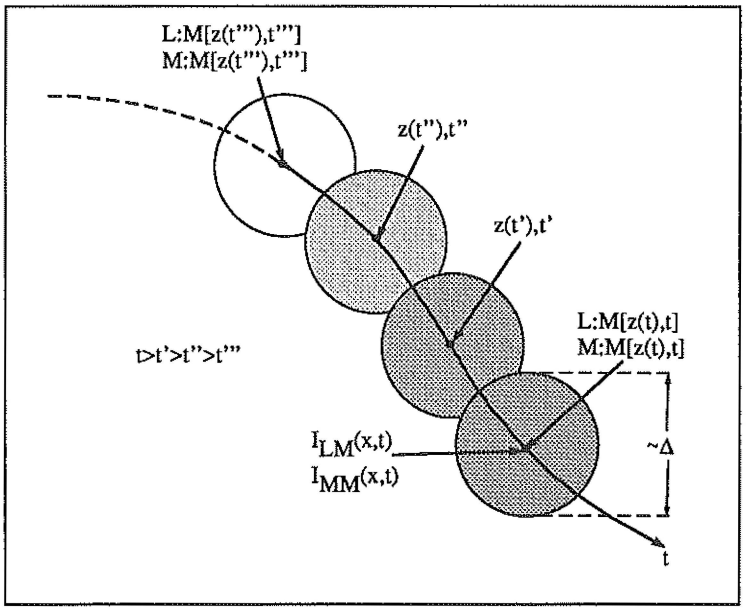

FIGURE 1. Sketch of fluid trajectory of the resolved LES velocity field. The error associated with the Germano identity is weighted with an exponentially decreasing function (indicated as different gray levels), backwards in time, to yield a current value for the model coefficient at point $\mathbf{x}$ and time t.

The function $W(t-t')$ is a free parameter in the current formulation, essentially defining the extent backward along the pathline over which we choose to minimize the error. Although several appropriate weighting functions are possible, an exponential weighting of the form $W(t-t') = T^{-1}e^{-(t-t')/T}$ has the distinct practical advantage that the integrals $\mathcal{I}_{LM}$ and $\mathcal{I}_{MM}$ are solutions to the following relaxation equations

$$\frac{D\mathcal{I}_{LM}}{Dt} \equiv \frac{\partial \mathcal{I}_{LM}}{\partial t} + \tilde{\mathbf{u}}\cdot\nabla\mathcal{I}_{LM} = \frac{1}{T}(L_{ij}M_{ij} - \mathcal{I}_{LM}), \tag{12}$$

$$\frac{D\mathcal{I}_{MM}}{Dt} \equiv \frac{\partial \mathcal{I}_{MM}}{\partial t} + \tilde{\mathbf{u}}\cdot\nabla\mathcal{I}_{MM} = \frac{1}{T}(M_{ij}M_{ij} - \mathcal{I}_{MM}). \tag{13}$$

In the context of LES, solving such transport equations is much more natural than having to perform integrals backwards in time according to Eqs. (10) and (11). Fig. 1 illustrates the basic idea of averaging over pathlines with an exponentially decreasing memory.

2.2 Relaxation time scale

The time-scale T controls the memory length of the Lagrangian averaging, and several choices can be made. The model coefficient should be responsive to changes that occur on the time-scales associated with the smallest resolved turbulent motions. Thus, one could choose T based on variables at the grid-scale. Some possible

choices are the following: (a) $T \sim |\tilde{S}|^{-1}$, (b) $T \sim |\overline{\tilde{S}}|^{-1}$, (c) $T \sim \Delta(M_{ij}M_{ij})^{-1/4}$, (d) $T \sim \Delta(L_{ij}M_{ij})^{-1/4}$, (e) $T \sim \Delta\mathcal{I}_{MM}^{-1/4}$, and (f) $T \sim \Delta\mathcal{I}_{LM}^{-1/4}$. In fully developed turbulence, all of these time-scales are of the same order of magnitude on average. The first four choices are based on local values, which would mean that T is a strongly fluctuating variable while (e) and (f) are based on the smoother, Lagrangian averages themselves.

Option (f) has several attractive features. Physically, it can be interpreted as a time scale for energy flux since it is formed by contracting a stress L with the strain-rate like tensor M. Thus, it may be indicative of the speed at which energy is being cascaded towards the grid-scale. Furthermore, if $L_{ij}M_{ij} \leq 0$ for a persistent time along the pathline, then $\mathcal{I}_{LM}$ approaches zero. T evaluated according to (f) then tends to ∞, i.e. the memory time increases. In other words, the current values are weighted less and less strongly relative to the past ones, if they are of the backscattering type. This is useful in the implementation with the Smagorinsky model where we wish to restrict the Smagorinsky expression for the modeling of energy dissipation only. The Germano identity is thus weighted much less heavily when $L_{ij}M_{ij} \leq 0$ in a persistent fashion, i.e. we opt for 'learning' as little as possible about the coefficient from the resolved field when it would predict backscatter.

Equation (12) can now be written as

$$\frac{D\mathcal{I}_{LM}}{Dt} = \frac{\theta}{\Delta}\,\mathcal{I}_{LM}^{\frac{1}{4}}\,(L_{ij}M_{ij} - \mathcal{I}_{LM}), \tag{14}$$

where θ is a dimensionless coefficient of order unity. If $\mathcal{I}_{LM}$ reaches zero, its rate of change is zero as well. Therefore, $\mathcal{I}_{LM}$ cannot become negative, and the resulting dynamic model will not suffer from numerical instability due to negative-eddy viscosities. We point out, however, that if $L_{ij}M_{ij} \leq 0$, the approach of $\mathcal{I}_{LM}$ to zero is not exponential, but of the power-law type (as $(t_0 - t)^{4/3}$). This means that after the (finite) time t_0 at which $\mathcal{I}_{LM} = 0$, the solution becomes complex. Thus, in practice, the solution must still be 'clipped' to zero during such times. This type of clipping is much less drastic than previous approaches since the coefficient field approaches zero smoothly with zero slope.

A judicious choice for the dimensionless coefficient θ must now be made. Intuitively, we must average over a few 'events' of the variable $L_{ij}M_{ij}$ along the pathline. The average duration of such events is expected to be of the order of $\Delta < L_{ij}M_{ij} >^{-\frac{1}{4}}$, but in order to quantify this assertion, we analyze results from DNS of forced isotropic turbulence. The goal is to compute the Lagrangian autocorrelation function of the scalar variable $L_{ij}M_{ij}$. The method employed to follow fluid trajectories and to compute the autocorrelation is the same as described in Meneveau & Lund (1994). For comparison, we also compute the Lagrangian autocorrelation function of the scalar $|\mathrm{M}|^2$ as well as their Eulerian fixed-point two-time autocorrelation functions. The Lagrangian tracking was done in a sequence of DNS velocity fields computed on a 128^3 mesh. The ensemble has a microscale Reynolds number of $R_\lambda = 95.8$. Each field was filtered with a Fourier cutoff filter at a scale corresponding to 4 mesh spacings. Lagrangian and Eulerian autocorrelations were then computed for quantities derived from the filtered velocity fields.

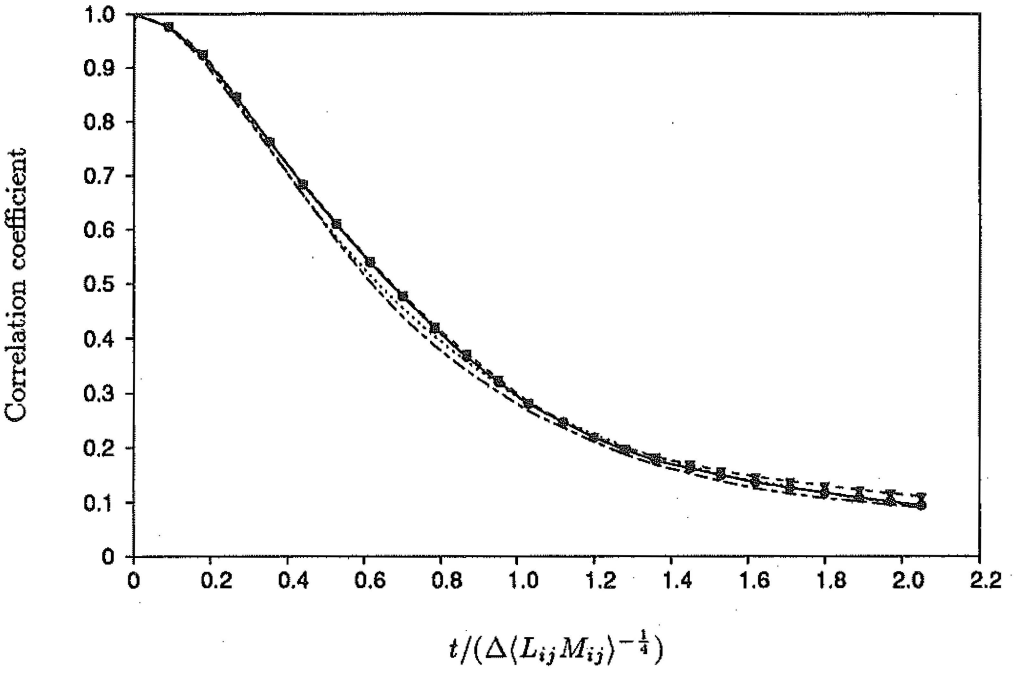

FIGURE 2. Lagrangian and Eulerian autocorrelation functions calculated from a filtered DNS of forced isotropic turbulence. • : Lagrangian autocorrelations of $L_{ij}M_{ij}$; ▲ : Lagrangian autocorrelations of $M_{ij}M_{ij}$; ——— : Eulerian temporal autocorrelations of $L_{ij}M_{ij}$; ····· : Eulerian temporal autocorrelations of $M_{ij}M_{ij}$.

Fig. 2 shows the computed autocorrelations. Time is non-dimensionalized based on the space-averaged value of $L_{ij}M_{ij}$. As expected, the Lagrangian autocorrelations decay at a slower rate than the Eulerian ones, but the difference is small due to the fact that the mean velocity of this flow is zero. Also, the decay of the LM and MM terms is quite similar. The main observation is that after a time $\sim 2\Delta < L_{ij}M_{ij} >^{-\frac{1}{4}}$, the autocorrelation almost vanishes. This suggests that averaging over Lagrangian time spans equal to this interval is sufficient to smooth instantaneous fluctuations. In summary, during the present work we choose

$$T = 2\ \Delta\ \mathcal{I}_{LM}^{-\frac{1}{4}} \tag{15}$$

as the time-scale characterizing the exponential memory with which the Germano identity is enforced.

2.3 Numerical method

In principle, the implementation of the Lagrangian dynamic model requires the solution of two additional transport equations (Eqs. (12) and (13)) during the LES. This undoubtedly increases the computational cost associated with the subgrid modeling. However, the considerable flexibility of choice of the averaging domain

suggests that high numerical accuracy in solving Eqs. (12) and (13) may be unnecessary. Therefore, we use a particularly simple formulation based on discretizing Eq. (12) in time as follows:

$$\frac{\mathcal{I}_{LM}^{n+1}(\mathbf{x}) - \mathcal{I}_{LM}^{n}(\mathbf{x} - \tilde{\mathbf{u}}^n \Delta t)}{\Delta t} = \frac{1}{T^n} \left([L_{ij} M_{ij}]^{n+1}(\mathbf{x}) - \mathcal{I}_{LM}^{n+1}(\mathbf{x}) \right). \tag{16}$$

Eq. (13) is dealt with in a similar manner. Positions $\mathbf{x}$ are coincident with grid points of the simulation. The value of $\mathcal{I}_{LM}^{n}$ at the previous time-step and at the upstream location $\mathbf{x} - \tilde{\mathbf{u}}^n \Delta t$ can be obtained by multilinear interpolation. Finally, the new values at the grid points are solved for. The result is a weighted sum of the interpolated prior value and the current source term at the grid point:

$$\mathcal{I}_{LM}^{n+1}(\mathbf{x}) = H \left\{ \epsilon \, [L_{ij} M_{ij}]^{n+1}(\mathbf{x}) + (1 - \epsilon) \mathcal{I}_{LM}^{n}(\mathbf{x} - \tilde{\mathbf{u}}^n \Delta t) \right\} \tag{17}$$

and

$$\mathcal{I}_{MM}^{n+1}(\mathbf{x}) = \epsilon \, [M_{ij} M_{ij}]^{n+1}(\mathbf{x}) + (1 - \epsilon) \mathcal{I}_{MM}^{n}(\mathbf{x} - \tilde{\mathbf{u}}^n \Delta t),$$

where

$$\epsilon \equiv \frac{\Delta t / T^n}{1 + \Delta t / T^n}, \quad \text{and} \quad T^n = 2 \, \Delta \, (\mathcal{I}_{LM}^{n})^{-\frac{1}{4}}, \tag{18}$$

where $H\{x\}$ is the ramp function ($H\{x\} = x$ if $x \geq 0$, and zero otherwise). The ramp function is introduced to clip the solution away from complex values.

Finally, we point out that the process of spatial interpolation between grid points introduces some numerical diffusion to the fields $\mathcal{I}_{LM}$ and $\mathcal{I}_{MM}$. Physically, such diffusion effectively 'thickens' the pathline over which the averaging is being performed, but this would not seem to be a worrisome aspect for this model.

2.4 Statistical features of the model

As a next step, the model is implemented in a LES for the simulation of forced isotropic turbulence on a 32^3 grid. The code is a variant of the pseudo-spectral method developed by Rogallo (1981). Forcing is achieved by holding the Fourier amplitudes fixed within the sphere $k < 2$. Test filtering is achieved through a Fourier cutoff at twice the grid scale.

The velocity field is initialized in the usual manner by superposing Fourier modes with a prescribed spectrum but random phases, and projection onto the divergence-free space. Additionally, initial condition for the fields $\mathcal{I}_{LM}$ and $\mathcal{I}_{MM}$ must be prescribed. For initializations corresponding to turbulent flows, we propose to set

$$\mathcal{I}_{MM}(\mathbf{x}, 0) = M_{ij} M_{ij}(\mathbf{x}, 0), \quad \mathcal{I}_{LM}(\mathbf{x}, 0) = c_s^2(0) \, M_{ij} M_{ij}(\mathbf{x}, 0), \tag{19}$$

where $c_s(0) = 0.16$ is the traditional value of the Smagorinsky constant. Thus at the initial time, the model involves a position-independent, prescribed coefficient.

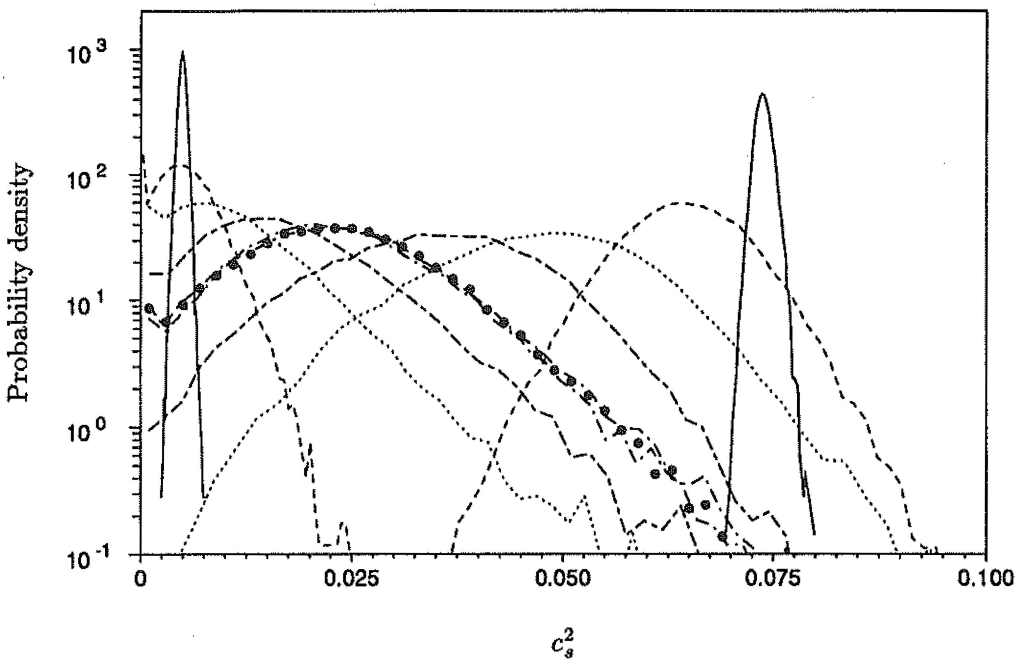

FIGURE 3. Probability density functions of the coefficient c_s^2, computed from the Lagrangian dynamic model in a pseudo-spectral LES of forced isotropic turbulence at $Re = \infty$, on a 32^3 mesh. The circles represent the asymptotic pdf long after initial transients have died out (obtained here at $t = 6 < T >$, where $< T >= 2\Delta < L_{ij}M_{ij} >^{-1/4}$). Evolving pdfs on both sides illustrate delta function pdfs with the wrong initial conditions quickly reach the asymptotic statistics. Curves that peak to the left of the asymptotic curve correspond to $c_s^2(0) = 0.005$; those peaking to the right evolve starting from $c_s^2 = 0.075$. ——— : (1 time-step); - - - - : $(t = 0.1 < T >)$; ····· : $(t = 0.45 < T >)$; — — — : $(t = 0.95 < T >)$; —·— : $(t = 1.9 < T >)$. For reference, in this simulation the time scale associated with the resolved strain-rates was $< \tilde{S}_{ij}\tilde{S}_{ij} >^{-1/2} = 0.26 < T >$.

For initializations corresponding to laminar flows, we propose to set $c_s = 0$ in the above expressions.

When the LES of forced isotropic turbulence is started, fluctuations of the Lagrangian dynamic coefficient c_s quickly build as different values of $L_{ij}M_{ij}$ begin to affect the averages. Once a statistical steady-state has been reached, these fluctuations are characterized by the probability density function of the coefficient shown by solid circles in Fig. 3. Notice the small spike at $c_s = 0$, arising from the regions in which c_s is clipped at zero, away from complex values (on about 5% of the points in this case). Initial transients leading to such a steady-state distribution are relatively short. This can be appreciated by observing the time development of the pdfs when the 'wrong' initial condition is employed for $c_s(0)$. In one case, we start with

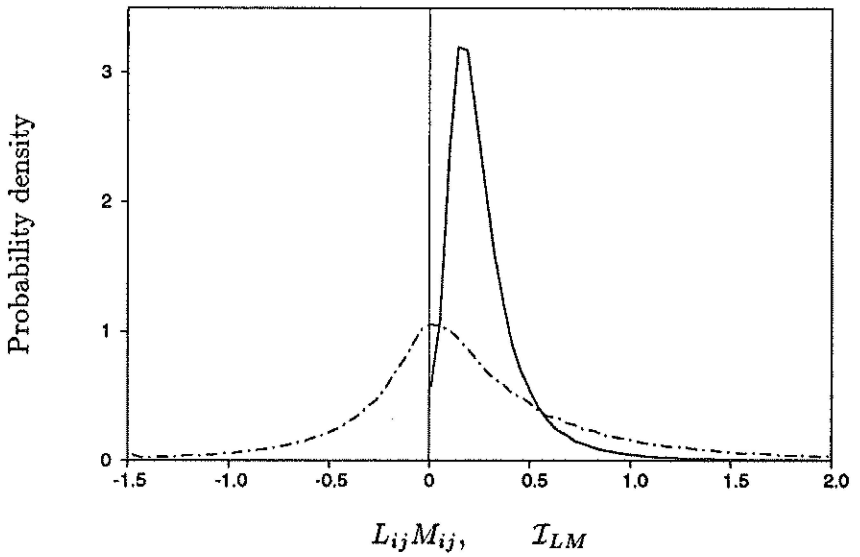

FIGURE 4. Probability density functions of numerators. —·— : evaluated locally ($L_{ij}M_{ij}$); ——— : after Lagrangian averaging ($\mathcal{I}_{LM}$). These distributions are calculated from a 32^3-node, pseudo-spectral LES of forced isotropic turbulence that uses the Lagrangian dynamic Smagorinsky model. To increase the sample, pdfs are accumulated over several independent fields.

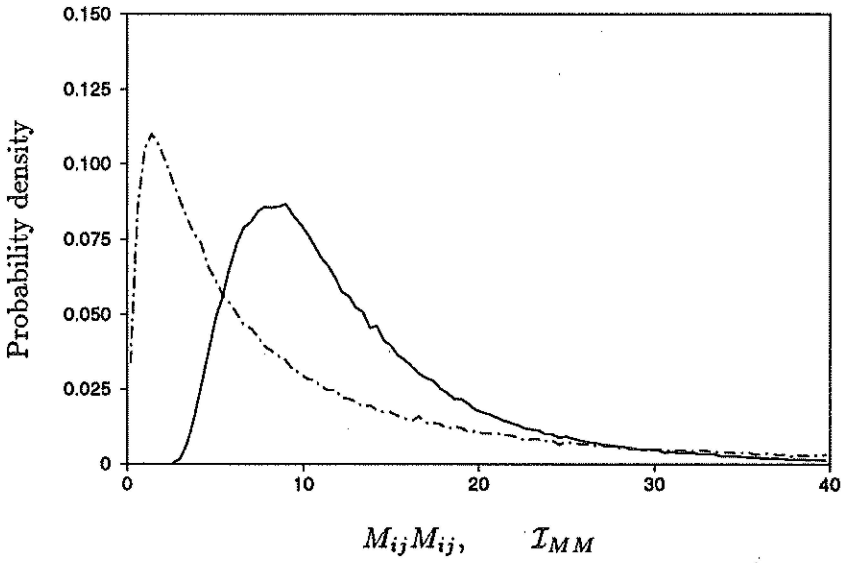

FIGURE 5. Probability density functions of denominators. —·— : evaluated locally ($M_{ij}M_{ij}$); ——— : after Lagrangian averaging ($\mathcal{I}_{MM}$). Details as in Fig. 4.

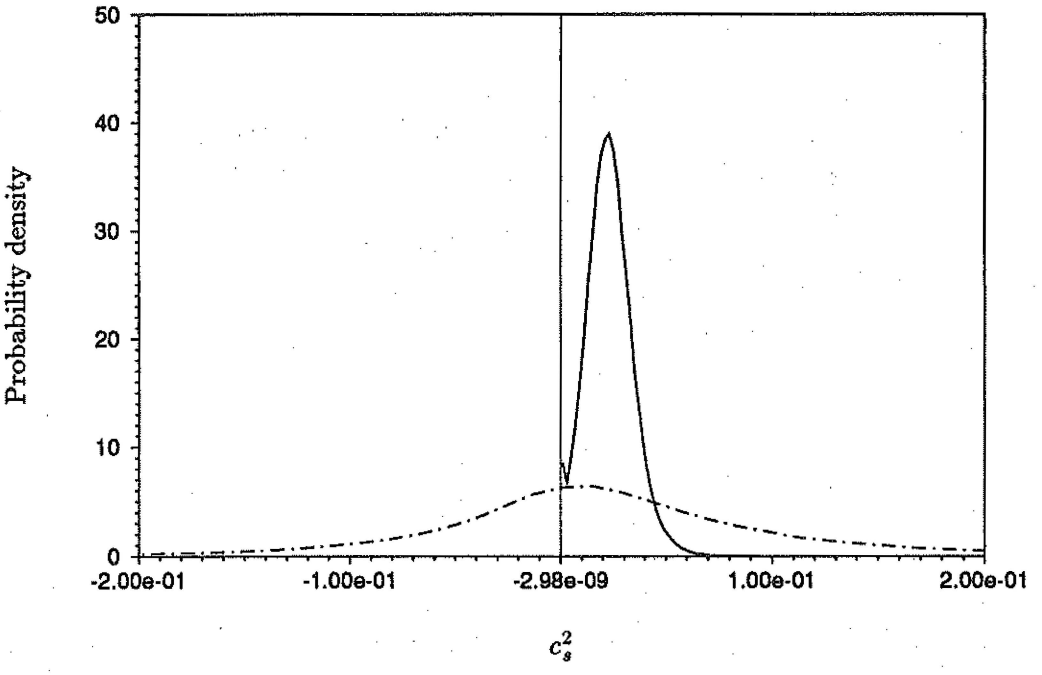

FIGURE 6. Probability density functions of model coefficients taken from a 32^3 Lagrangian dynamic model LES of forced isotropic turbulence. —·— : coefficient evaluated locally; ——— : coefficient from the Lagrangian model.

$c_s^2(0) = 0.005$, and in another case with $c_s^2(0) = 0.075$. In both cases the asymptotic distribution is reached after times of the order of $2 < T >$ where T is the time scale defined by Eq. (15). We conclude that the proposed method of initialization is acceptable since the simulation 'forgets' the initial state after only few grid-scale turnover times. This is comparable to the time it takes the simulation to build up realistic phases in the resolved velocity field, starting from the random-phase initial condition. To further document the effect of the Lagrangian averaging, we compute the probability density functions of $\mathcal{I}_{LM}$ and $\mathcal{I}_{MM}$ and compare them with those of the local values $L_{ij}M_{ij}$ and $M_{ij}M_{ij}$. Figs. 4 and 5 show these results. As expected, the distributions become narrower after the Lagrangian averaging. By construction, there are no negative values of $\mathcal{I}_{LM}$ (Fig. 4). In terms of denominators, the averaging is seen to virtually eliminate values near zero. The pdf of $\mathcal{I}_{MM}$ approaches the origin with negligible slope while the probability of the local value of $M_{ij}M_{ij}$ being close to zero is considerable. In Fig. 6, we show the measured pdf of the coefficient c_s^2 itself. As can be seen, the variance of the coefficient in the local formulation is greatly reduced by the Lagrangian averaging. Also, no negative values exist although a finite number of points ($\sim 5\%$) exhibit $c_s^2 = 0$ as indicated by the spike at the origin.

2.5 Relationship to vortical flow-structures

The goal of this section is to make qualitative observations pertaining to possible relations between the terms $\mathcal{I}_{LM}$, $\mathcal{I}_{MM}$, and discernible flow structures that may appear in the resolved velocity field during LES.

First, we report the existence of tubular structures that characterize regions in which the resolved vorticity vector has high magnitude, in our 32^3 LES. Fig. 7a shows iso-surfaces of vorticity magnitude (at a threshold of $|\omega|_{th} = 2.4 < \omega^2 >^{1/2}$). Clearly, 'fat worms' exist in the solution. The existence of tubular vortical structures in LES has also been observed recently by Briscolini and Santangelo (1994), using a different subgrid model. One interesting question to be answered is whether the prediction of such 'fat worms' by LES is realistic. We recall that DNS predicts worms with very small diameters of about four Kolmogorov scales (Jimenez *et al.*, 1993)). Surely they cannot be captured by a LES at $Re = \infty$. The relevant question is whether a field generated by DNS and then low-pass filtered at inertial-range scales comparable to the LES grid-size exhibits 'fat worms' that are comparable to those predicted by LES. We have performed such an operation based on the 128^3 forced DNS described earlier and have visualized regions of high vorticity-magnitude. We indeed observed 'fat worms' that were of similar appearance than those of the LES (see also Fig. 17 of Vincent & Meneguzzi, 1991). It must be recognized that the 'high-vorticity' regions in the filtered DNS correspond to much lower vorticity-magnitudes than those of the unfiltered fields. This is the reason why these 'fat worms' are not visible when analyzing the unfiltered DNS fields. In summary, we observe elongated vortical regions in LES and believe that their existence is a realistic prediction by the simulation since they also exist in low-pass filtered DNS fields.

The next issue to be addressed is whether the Lagrange-averaged quantities that enter our dynamic model bear any relationship to such local structures. Fig. 7(a) shows contour plots of $\mathcal{I}_{LM}$ on two planes of the computational cube, selected to cut some of the most visible vortical structures. The field is chosen at some time *long* after the simulation has reached statistical steady-state (15,000 time-steps). Fig. 7(b) shows a similar graph for $\mathcal{I}_{MM}$. Generally, it is apparent the contours of both $\mathcal{I}_{LM}$ and $\mathcal{I}_{MM}$ are somewhat 'correlated' with the presence of worms. The contours peak in the neighborhood of the worms while not much activity is seen in regions that are far removed from the structures. Upon closer examination, we observe that the peaks in $\mathcal{I}_{LM}$ and $\mathcal{I}_{MM}$ are most often located near the cores of the worms but not inside of them. Many times the maximum values occur between two closely spaced worms. These are expected to be regions of large straining and turbulence generation. Also, considerable correlation is seen between both fields $\mathcal{I}_{LM}$ and $\mathcal{I}_{MM}$ (it is $\rho(\mathcal{I}_{LM}, \mathcal{I}_{MM}) \sim 0.8$ while the correlation between the local values is much lower, $\rho(L_{ij}M_{ij}, M_{ij}M_{ij}) \sim 0.4$). This increased correlation between numerator and denominator is instrumental in decreasing the variance of the predicted model coefficient.

Clearly, a detailed understanding of the relationship between the coefficient c_s^2 and local flow structures, and of their dynamical interplay and relevance, is still

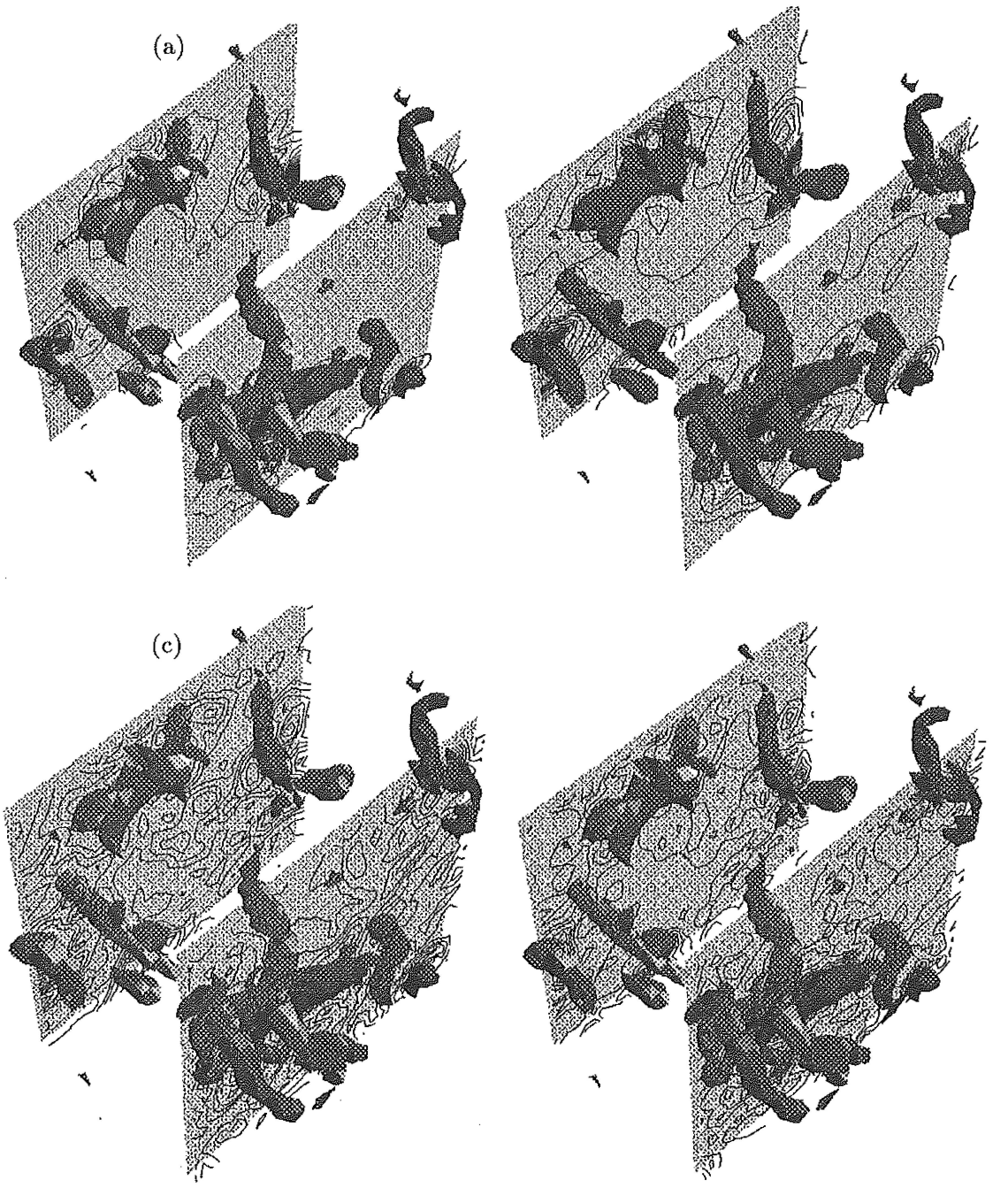

FIGURE 7. Visualization of high-magnitude vorticity regions in LES of isotropic forced turbulence at $Re = \infty$. Surfaces correspond to points at which $|\tilde{\omega}| = 2.4 < \tilde{\omega}^2 >^{1/2}$. On planes, contours of different variables shown. (a) $\mathcal{I}_{LM}$, (b) $\mathcal{I}_{MM}$, (c) $|\tilde{S}|$ (proportional to eddy viscosity with volume-averaged coefficient) and (d) $(\mathcal{I}_{LM}/\mathcal{I}_{MM})\ |\tilde{S}|$ (proportional to eddy viscosity computed from Lagrangian dynamic model).

elusive. Nevertheless, we have shown that the Lagrangian averaging preserves some spatial locality in the model. Spatially localized events in the numerators and denominators used to compute the model coefficient bear some relationship to local flow structures. The volume-averaged dynamic model would have generated a position-independent coefficient that is oblivious to local flow structures. To observe the effect on the predicted eddy viscosity, Figs. 7(c) and 7(d) show contour plots of the strain-rate magnitude $|\tilde{S}|$ and of the expression $(\mathcal{I}_{LM}/\mathcal{I}_{MM})|\tilde{S}|$. The former is proportional to the eddy viscosity predicted with a volume averaged coefficient while the latter is proportional to the eddy viscosity predicted by the Lagrangian dynamic model. Both show peaks surrounding the worms, but the precise location of these peaks differs. Also, the Lagrangian dynamic eddy viscosity appears to be more intermittent in the sense that more eddy viscosity is concentrated near the structures while being lower and fluctuating less in the regions far away from the structures.

3. Applications

In this section, we report applications of the Lagrangian dynamic model to several test-cases. We consider forced and decaying isotropic turbulence and channel flow. These flows could have also been treated with the traditional dynamic model with averaging over statistically homogeneous directions (and they have in the past). Our purpose in choosing these simple flows is to test the model in well-understood cases and show that good results can be obtained. This is a necessary first step before applications to unsteady and complex-geometry flows should be attempted where many other effects such as numerics, etc. may influence the results and obscure the role of the subgrid model.

3.1 Forced isotropic turbulence

LES of forced isotropic turbulence is performed on both 32^3 and 128^3 grids, using the code already described in section 2.4. The simulation is run for 15,000 and 6,600 time-steps on the 32^3 and 128^3 grids, respectively.

Figs. 8(a) and 8(b) show the resulting radial energy spectra. The wavenumbers and energy density are made dimensionless with the grid wavenumber and the averaged subgrid-scale energy dissipation $(- < \tilde{S}_{ij}\tau_{ij} >)$. Figure 8(b) is premultiplied by $k^{5/3}$. In these 'mesh-Kolmogorov units', one expects simulations with different meshes to collapse at high wavenumbers, and the spectra to follow the universal power-law in the inertial range. The dotted line in Fig. 8(a) shows a power-law $(k/k_\Delta)^{-5/3}$. A slight decay below the power law for $k/k_\Delta > 0.3$ and a 'pile-up' very close to the cut-off wavenumber k_Δ are visible. These are known effects of physical space eddy viscosity closures, which do not have a 'cusp' near k_Δ. These defects appear not to be remedied by the dynamic model in its Lagrangian implementation. We have confirmed that the same is true for the traditional dynamic model by running the same program with the volume-averaged dynamic coefficient.

With regard to computational cost, we find that the CPU time for the simulation with the Lagrangian averaging was higher by about 9% when compared to that of the volume-averaged dynamic model. Most of the additional time was spent in the

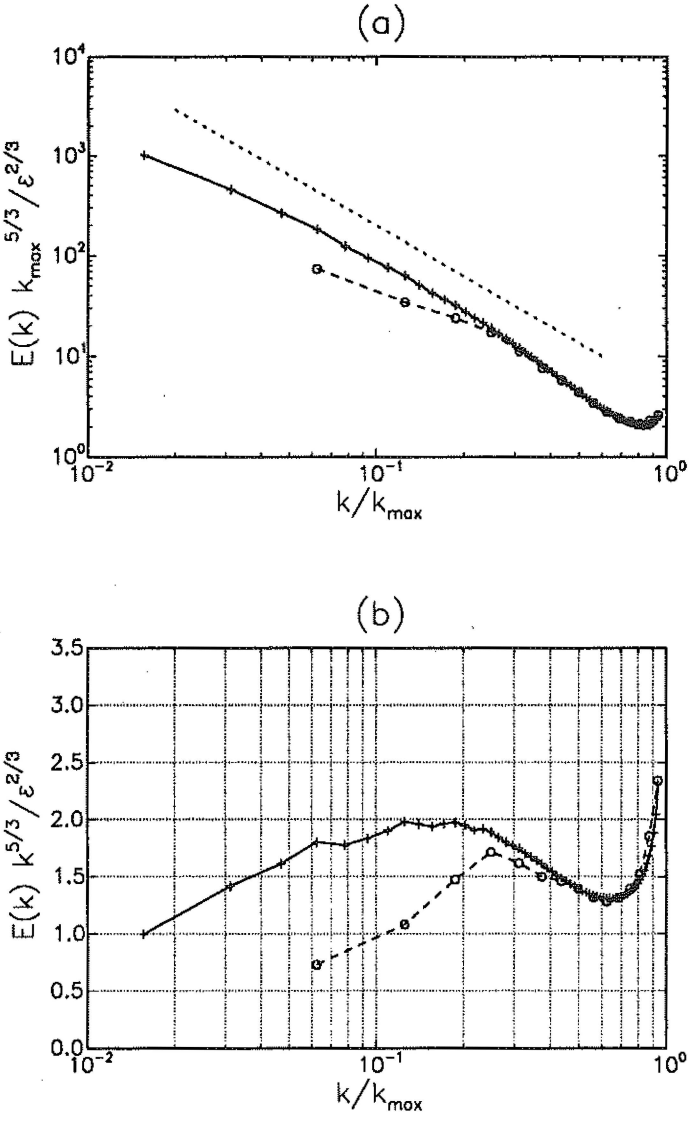

FIGURE 8. Radial energy spectra of LES using Lagrangian dynamic Smagorinsky model at $Re = \infty$. Wavenumbers are non-dimensionalized with grid-wavenumber while non-dimensionalization of energy density also involves mean subgrid-scale energy dissipation rate, $\epsilon = - < \tau_{ij} \tilde{S}_{ij} >$, computed from simulation. (a) conventional spectra, (b) premultiplied spectra. ——— : 128^3 simulation; ---- : 32^3 run; ····· : slope $-5/3$. 32^3 spectrum averaged over 374 independent samples taken from 15,000 time-steps (approximately 13 integral large-scale turnover times L/u', with $L = 2\pi$). The 128^3 spectrum is based on 290 samples taken from 6,600 time-steps (approximately 4 large-scale turnover times).

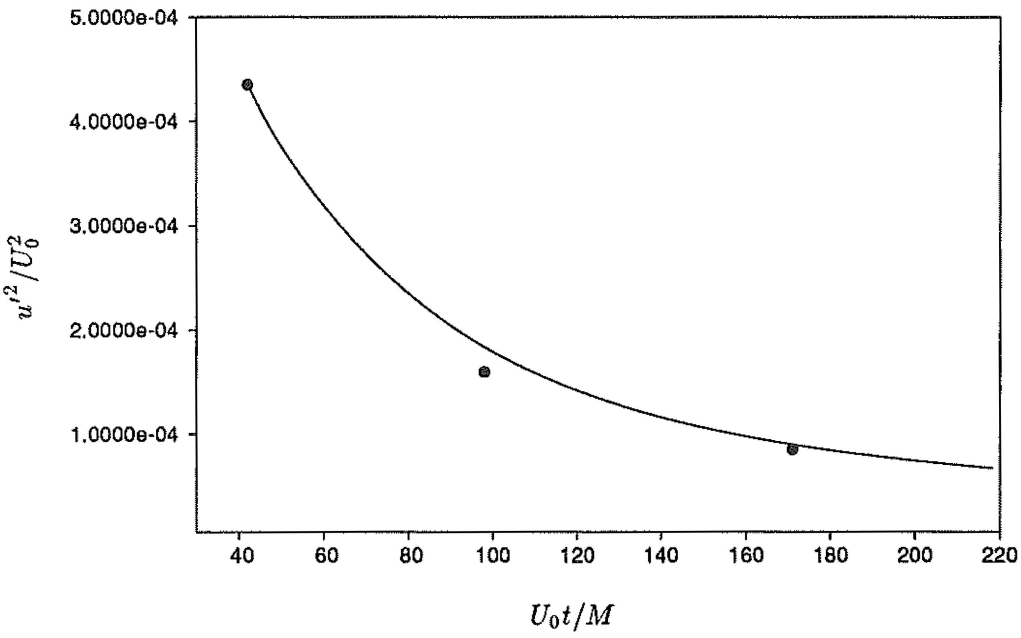

FIGURE 9. Temporal decay of turbulent kinetic energy in isotropic turbulence. ——— : 32^3 LES using the Lagrangian dynamic model; • : filtered experimental results (Comte-Bellot & Corrsin, 1971) in grid turbulence which decays downstream of a grid. U_0 and M are the mean fluid speed and the spacing of the turbulence-generating grid in the experiment.

linear interpolations. Two additional scalar arrays had to be defined, for $\mathcal{I}_{LM}$ and $\mathcal{I}_{MM}$. Compared to overall memory requirements, this addition was not significant.

3.2 Decaying isotropic turbulence

In order to test the model in an unsteady case, we perform LES of decaying isotropic turbulence. Meaningful comparisons can then be made with the experimental results of Comte-Bellot & Corrsin (1971). The initial 3-D energy spectrum is made to match the experimental measurements at their earliest time. The phase of the Fourier coefficients is chosen to be random so that the initial velocity field had Gaussian statistics. The dimension of the computational box is chosen to be roughly 4 integral scales.

Fig. 9 shows the decay of the kinetic energy compared with the experimental results of Comte-Bellot & Corrsin (1971). The predicted initial decay appears to be a little slower than the experimental rate, but the overall agreement is good. Of course the agreement could have been improved by using a slightly larger value of $c_s^2(0)$ as initial condition - an after-the-fact adjustment that we opted to avoid. A comparison of the spectra at the three different times at which experimental results are available is shown in Fig. 10. The decrease in overall kinetic energy and the decrease of k at which the spectra peak (increasing integral scale) is clearly

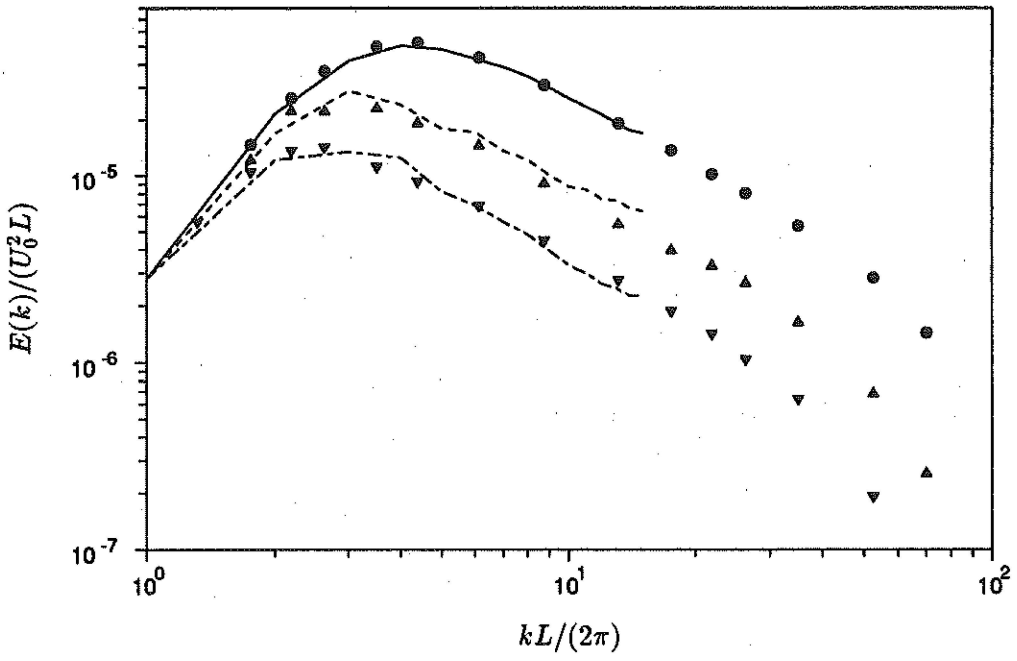

FIGURE 10. Radial energy spectra for decaying isotropic turbulence at different times. ——— : 32^3 LES with Lagrangian dynamic model; ● : experimental results of Comte-Bellot & Corrsin (1971). Scaling parameters are defined in Fig. 9. $L = 10.8M$ is the computational box size.

reproduced well.

We conclude that the model is able to reproduce important features of this time-dependent flow.

3.3 Fully developed channel flow

In this section we describe the application of the Lagrangian dynamic model to a pseudo-spectral simulation of plane channel flow. For comparison, another LES is performed with the traditional implementation of the dynamic model in which the terms are averaged over planes parallel to the wall. The flow Reynolds number is selected to match the experimental data by Hussain & Reynolds (1970) to permit detailed comparison.

The channel flow simulations are performed with in a pseudo-spectral code (Kim *et al.*, 1987) in a numerical domain with streamwise, wall-normal, and spanwise dimensions of $3\pi \times 2 \times 3\pi/4$ (in units of channel half-width d) on a $48 \times 65 \times 64$ mesh. Chebyshev polynomials are used in the wall-normal direction on a collocated grid; Fourier transforms are used in the homogeneous streamwise and spanwise directions on a uniform grid. Real space (tophat) filtering is used for the dynamic test filtering procedure and is performed explicitly only in horizontal planes. The equivalent filter width Δ_{eq} is taken to be the geometric mean of unidirectional grid

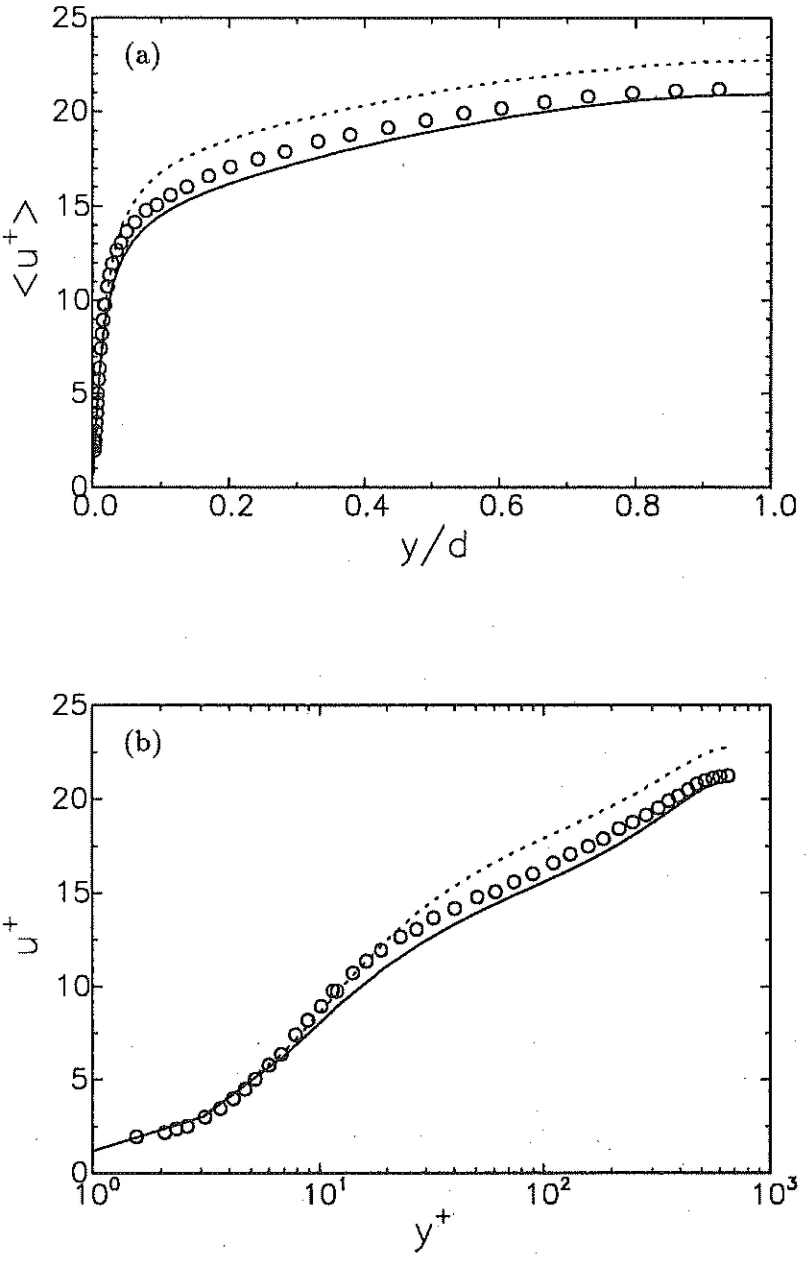

FIGURE 11. Mean velocity profiles in fully developed channel flow. ····· : LES with plane-averaged dynamic model; —— : LES with Lagrangian dynamic model; • : Experimental measurements of Hussain & Reynolds (1970). (a) Wall distance in units of the half-channel width d, (b) in wall units.

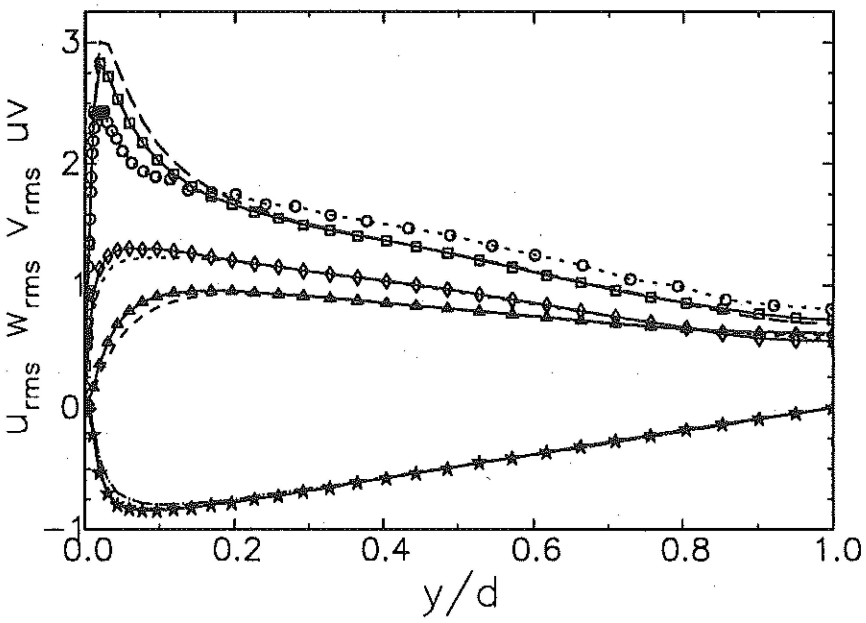

FIGURE 12. Profiles of second-order moments of the resolved velocity field. ---- : u'_{rms} from the plane-averaged LES; □ : u'_{rms} from Lagrangian model; ○ : u'_{rms} from the experimental measurements of Hussain & Reynolds (1970). ◇ : Spanwise w'_{rms} from Lagrangian LES; ····· : from plane-averaged model. △ : Wall-normal v'_{rms} from Lagrangian LES; ---- : from plane-averaged model. ⋆ : Resolved shear stress $< u'v' >$ from Lagrangian LES; —·— : from plane-averaged model.

widths (this procedure is justified for moderate grid anisotropies as shown in Scotti *et al.*, 1993). For the plane-averaged LES, averaging of the dynamic coefficient is performed in horizontal planes.

The approximate Lagrangian interpolation for the horizontal directions is implemented in this code as described in §2.3. The wall-normal direction requires different treatment due to the stretched mesh used in that direction. The transformation $\theta = \cos^{-1}(y/d)$ is used to map the stretched mesh into a uniform one. The wall-normal advection term, $v\partial/\partial y$, is recast as $v_\theta \partial/\partial\theta$ and the interpolation is performed in θ identically to the horizontal directions, but using $v_\theta = -v/\sin\theta$. The wall planes are treated specially with $\mathcal{I}_{LM} \equiv 0$ and $\mathcal{I}_{MM}$ approximated by values at the nearest off-wall plane. There was also the possibility that the interpolation might attempt to place approximated points at the previous time step beyond the walls; however, the CFL condition gives sufficiently small time steps that this situation is never encountered.

A target friction Reynolds number Re_τ ($\equiv u_\tau d/\nu$, where the friction speed u_τ

is the square root of the mean total wall stress, and ν is the molecular viscosity) of 650 was chosen, corresponding to one set of experimental data by Hussain & Reynolds (1970). The channel flow is started from a flow field at lower Reynolds number and is allowed to evolve to near statistical equilibrium, with $Re_\tau \approx 641$ in the last runs. The initial conditions for $\mathcal{I}_{LM}$ and $\mathcal{I}_{MM}$ are chosen as in the homogeneous case but with $c_s^2(0)$ as function of y matching the values of a previous plane-averaged dynamic simulation. Using the Lagrangian formulation proved to be more expensive than the standard plane-averaged method by 10% in CPU due, in part, for the need to perform a division at each point to compute the dynamic coefficient rather than at each plane. The Lagrangian method also requires extra mass storage of $\mathcal{I}_{LM}$ and $\mathcal{I}_{MM}$ between runs.

The averaged statistics will be shown first, followed by a more detailed analysis of additional variables.

Fig. 11 shows the mean velocity profile in the half-channel, in outer units (a) and wall units (b). As can be seen, at the resolution of the present LES, the plane-averaged model predicts an excessive center-line velocity (smaller losses) for the prescribed pressure gradient. The Lagrangian model yields a centerline velocity slightly below the measured values although the magnitude of the error is considerably smaller than that of the plane-averaged case (6.8% error in centerline velocity for the plane-averaged model and -1.8% for the Lagrangian model). Fig. 12 shows the profiles of *rms* velocities and Reynolds shear stress of the resolved fields, and a comparison of the *rms* streamwise velocity with the measurements of Hussain & Reynolds (1970). In the core region (for $y/d > 0.2$), the LES with both models fall below the measured values to a large extent because the former do not include the subgrid portion of the energy. Closer to the wall, both LES erroneously overpredict u'_{rms}, but the Lagrangian model does a better job than the plane-averaged one. Interestingly, the magnitude of the resolved shear stress for the Lagrangian model is larger than that of the plane-averaged case. This is possibly the cause for the increased (more realistic) losses in the Lagrangian simulation. The mean eddy viscosity predicted by both LES is shown in Fig. 13. It is computed according to

$$< \nu_t > (y) = < c_s^2(x,y,z,t)^2 \ \Delta_{eq} |\tilde{S}| >_{x,z}, \tag{20}$$

where the averaging is performed along x, z planes and over several times. The coefficient c_s^2 is either computed according to the plane-averaged or the Lagrangian dynamic model. It can be seen that over much of the log-layer, the Lagrangian model generates a lower eddy viscosity compared to the plane-averaged dynamic model. We have checked that this reduction is due primarily to a decrease in the dynamic coefficient c_s^2 as opposed to reduced strain-rate magnitudes. The reduced eddy viscosity is likely to generate less SGS dissipation of resolved turbulence, which in turn is probably the cause for the increased resolved shear-stress observed before.

As an aside, an important feature of the dynamic model is that it exhibits the proper near-wall scaling for the SGS eddy viscosity when the sublayer is numerically resolved (Germano *et al.*, 1991), namely $\nu_t \sim (y^+)^3$. As can be seen in Fig. 13, this scaling is followed quite well by the plane-averaged case (as observed before by

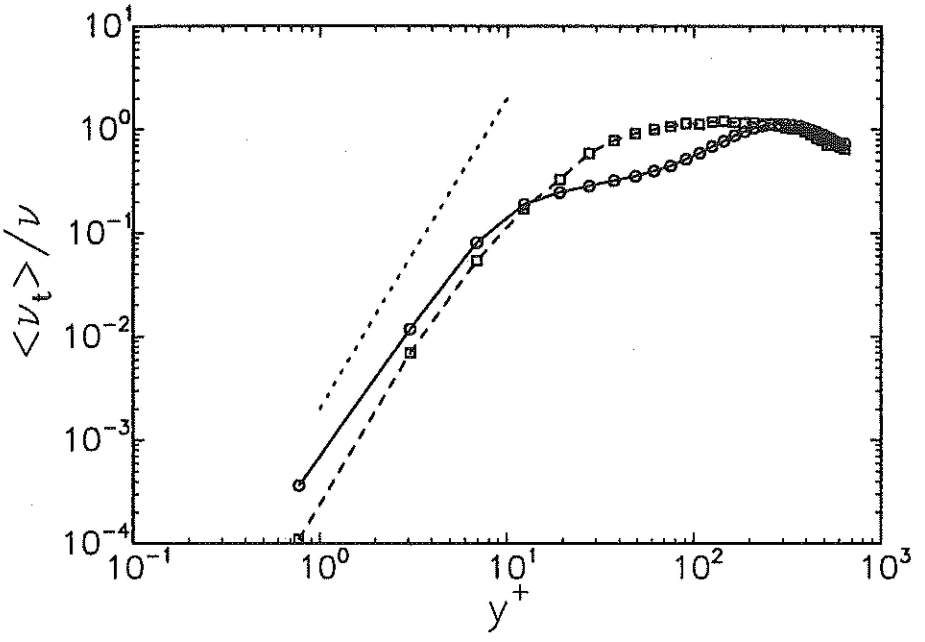

FIGURE 13. Ratio of mean eddy viscosity to molecular viscosity taken from the channel flow simulation. o : Lagrangian dynamic model; □ : plane-averaged dynamic model; ····· : $\nu_t \sim (y^+)^3$ power-law.

Germano *et al.* 1991; Piomelli, 1993). The mean eddy viscosity from the Lagrangian model also decays very quickly but at a somewhat slower rate (approximately as $\nu_t \sim (y^+)^{2.5}$ in our case). We shall return to this issue at a later stage. But we stress that near the wall such minute differences are unlikely to have any practical effect since there the molecular viscosity strongly dominates. With the purpose of documenting the statistics of the model coefficient c_s^2 and its evolution away from the initial condition, we show in Figs. 14(a)-(c) probability-density-functions of c_s^2 at different times and different elevations from the wall. The pdf at $t = 0$ is a *delta*-function at the plane-averaged value of the dynamic coefficient, which is used as an initial condition. As can be seen for $y^+ = 641$ and $y^+ = 12$ (core and near-wall region), the convergence of the pdf to the asymptotic value (circles) is nearly complete after 80-160 time-steps. This duration corresponds to about $\nu/u_\tau^2 \sim 25 - 50$ viscous times or $d/u_\tau \sim 0.04 - 0.08$ outer times. At $y^+ = 108$, the convergence is slower because in the log-layer the initial guess for c_s^2 is worst. Still, after between 300 and 600 time-steps, the asymptotic state is reached for the fluctuations in c_s^2. Figs. 14(b) and (c) clearly show the considerable decrease of typical c_s^2 values in the Lagrangian model as compared to the plane-averaged model.

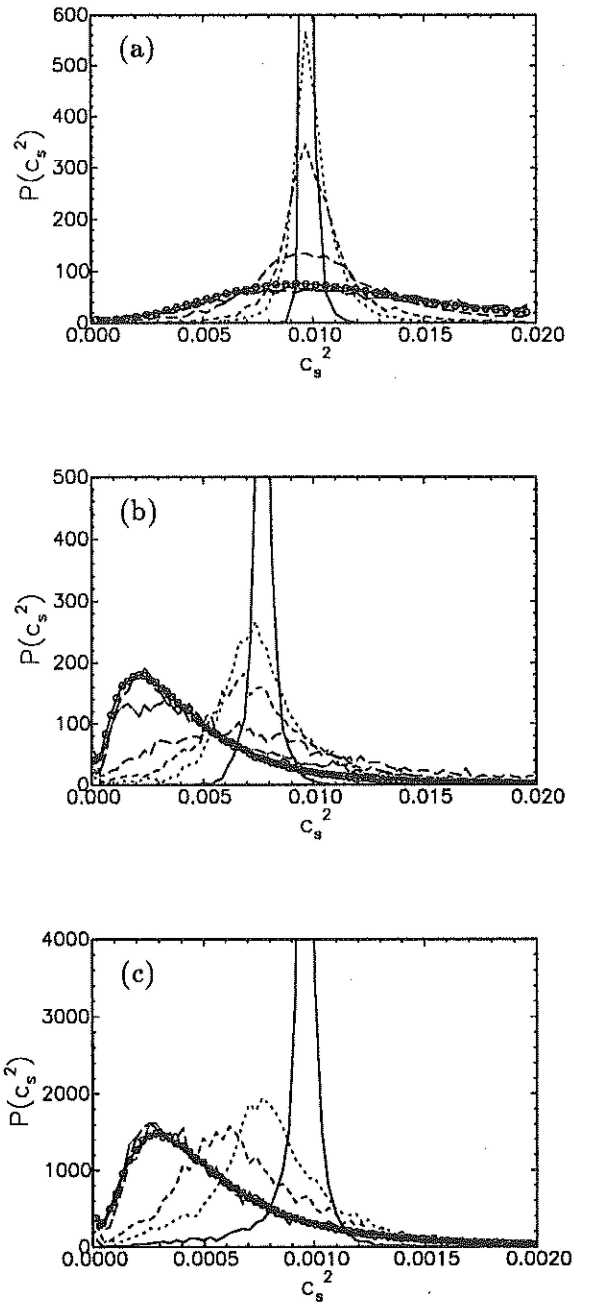

FIGURE 14. Probability-density functions of dynamic model coefficient c_s^2 for different time steps, n. ——— : n=2; ····· : n=10; - - - - : n=20; — — — : n=80; — — — : n=320; —·—·— : n=640; o : $n \sim 38,000$. Different graphs are at different heights above the wall: (a) is at $y^+ = 641$, (b) at $y^+ = 108$ and (c) at $y^+ = 12$.

LES – plane-averaged			
y^+	12	108	640
$< L_{ij}M_{ij} >$	$2.912\ 10^4$	$5.362\ 10^2$	$1.099\ 10^1$
$< M_{ij}M_{ij} >$	$3.054\ 10^7$	$4.932\ 10^4$	$6.998\ 10^2$
LES – local Lagrangian			
y^+	12	108	641
$< \mathcal{I}_{LM} >$	$2.690\ 10^4$	$7.076\ 10^2$	$1.056\ 10^1$
$< \mathcal{I}_{MM} >$	$2.814\ 10^7$	$2.537\ 10^5$	$7.777\ 10^2$

TABLE 1. Numerators and denominators in the expressions for the dynamic coefficients averaged over sample planes.

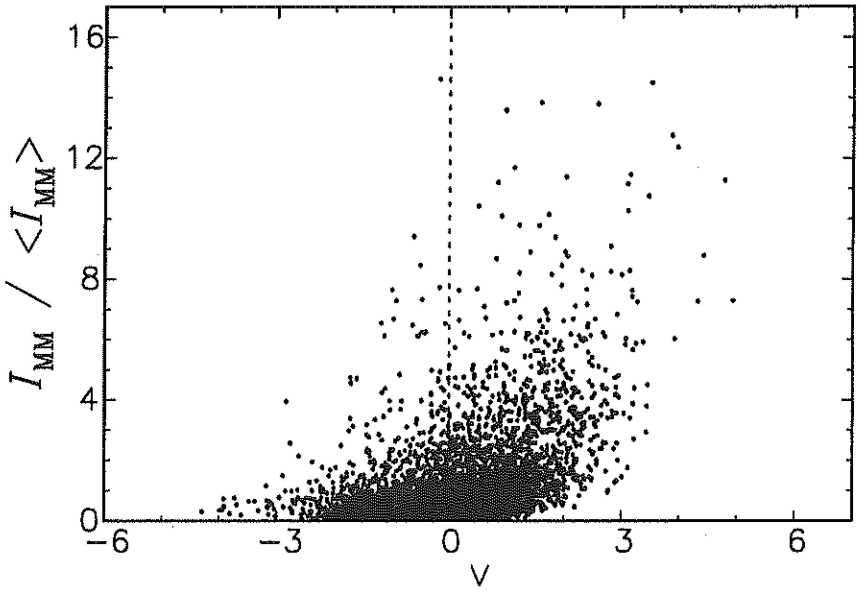

FIGURE 15. Scatter plot of $\mathcal{I}_{MM}$ versus vertical velocity v' in LES of channel flow, using the Lagrangian dynamic model.

The main issue left to answer is why the Lagrangian model generates such decreased coefficients in the log-layer. For this purpose, the average values of numerators and denominators are evaluated separately for both models on some sample planes as given in Table 1.

The largest discrepancy can be seen by comparing the denominators $< M_{ij}M_{ij} >$ and $< \mathcal{I}_{MM} >$ at $y^+ = 108$. A possible reason for this discrepancy can be deduced

by comparing $< M_{ij}M_{ij} >$ at $y^+ = 12$ and at $y^+ = 108$. $< M_{ij}M_{ij} >$ and $< \mathcal{I}_{MM} >$ are several orders of magnitude higher in the near-wall region, as is to be expected for a variable based on the strain-rate (to the fourth power). During ejection events, fluid particles that were close to the wall reach deep into the log-layer, thus convecting elevated values of $\mathcal{I}_{MM}$ upwards. This feature can be deduced from Fig. 15, which shows a scatter plot of the Lagrangian denominator $\mathcal{I}_{MM}$ as function of the local vertical velocity. Clearly, large values of $\mathcal{I}_{MM}$ are associated with positive values of v', which are indicative of ejection events or bursts.

The net effect is that the Lagrangian model is less dissipative as far as bursts are concerned. They can survive longer and feed more turbulence into the channel flow, producing more realistic (higher) levels of Reynolds-averaged (resolved) eddy viscosity and losses.

It is likely that a similar phenomenon causes the near-wall scaling of Lagrangian eddy viscosity to be less steep than that of the plane-averaged model. Occasionally, 'sweeps' bring log-layer material into the sublayer and effectively increase the model coefficient and eddy viscosity above that of the plane-averaged model. Numerical diffusion is also likely to play a role in reducing spatial differences in $\mathcal{I}_{LM}$ and $\mathcal{I}_{MM}$.

3.4 Transitional channel flow

A known drawback of the traditional eddy viscosity closure for LES of transitional flows is that it is overly dissipative, possibly eliminating instabilities altogether (Piomelli & Zang, 1990). The dynamic model, on the other hand, yields essentially zero eddy viscosity if the resolved part of the flow is not turbulent. Instabilities are thus allowed to grow initially in a realistic fashion, as shown in simulations of transitional channel flow using the dynamic model, with planar averaging (Germano *et al.*, 1991). Once the non-linear breakdown phase is reached, the SGS model must become active in order to prevent excessive growth of turbulent kinetic energy, wall shear-stresses, etc. In the Lagrangian model, the variable $\mathcal{I}_{\mathcal{LM}}$ must be initialized to zero everywhere in the laminar region. As turbulence is generated, this variable (and therefore the eddy viscosity) will rise from zero. The rate at which $\mathcal{I}_{\mathcal{LM}}$ rises from zero is controlled in part by the memory time scale. If the memory time scale, T, is too long, the rise in eddy viscosity may occur too late in the transition process. In order to investigate this potential problem, we have performed an LES of transitional channel flow. In this section we attempt to ascertain if the Lagrangian model as proposed here (with the time scale given by Eq. 15) is able to (i) allow for initial instabilities to grow in a realistic fashion, and then to (ii) sufficiently damp the turbulence at the appropriate time.

The transition channel case is identical to that of Zang *et al.* (1990), Piomelli & Zang (1991) and Germano *et al.* (1991). The initial (laminar) centerline Reynolds number is 8,000. The initial condition consists of a parabolic mean flow plus a 2-D Tollmien-Schlichting wave of 2% amplitude and a pair of 3-D Tollmien-Schlichting waves of 0.02% amplitude. The streamwise wavenumber for both the 2-D and 3-D modes is 1.0, whereas the spanwise wavenumber for the 3-D modes is ± 1.5. See Zang *et al.* (1990) for more details on the initial conditions. The dimensions of the computational domain (streamwise, wall-normal, and spanwise) are $2\pi \times 2 \times 4\pi/3$

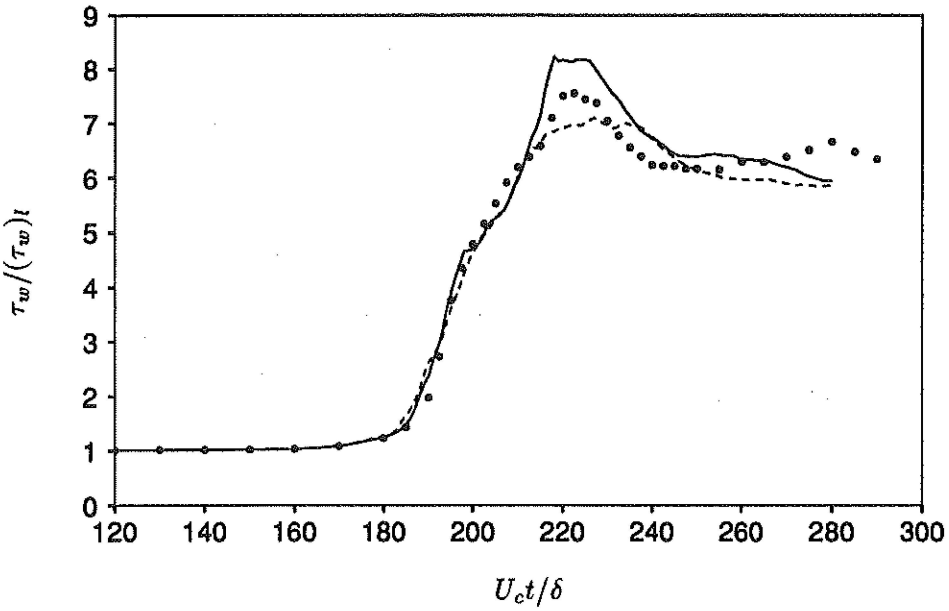

FIGURE 16. Time history of wall-shear stress from the transitional channel simulation. ——— : Lagrangian model LES; - - - - : plane-averaged dynamic model LES; ● : DNS of Zang *et al.* (1990).

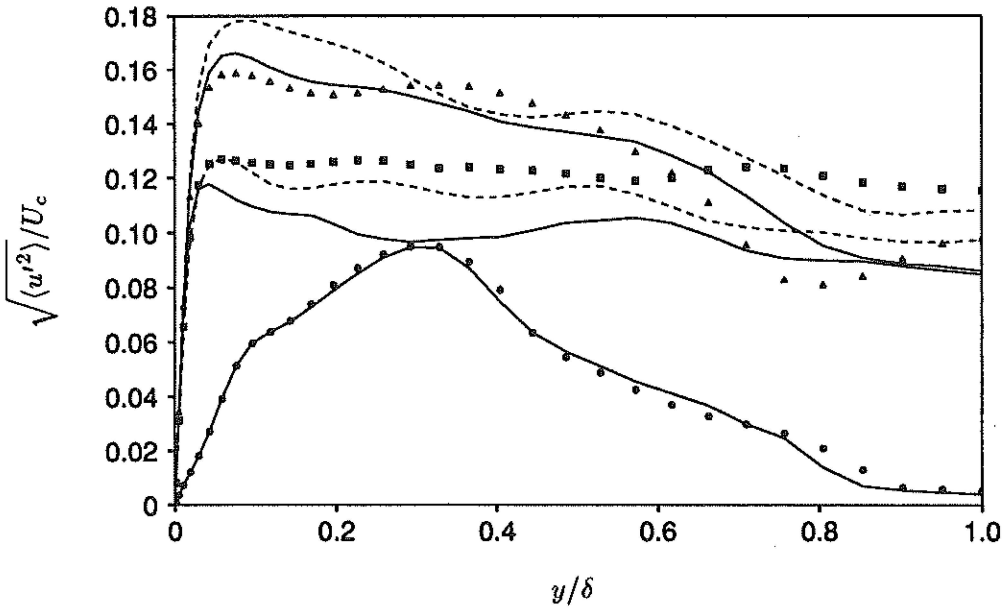

FIGURE 17. Streamwise velocity fluctuation profiles from the transitional channel flow simulation. Symbols: DNS of Zang *et al.* (1990). ● : $t = 176$; ▲ : $t = 200$; ■ : $t = 220$; ——— : Lagrangian model LES; - - - - : plane-averaged dynamic model LES.

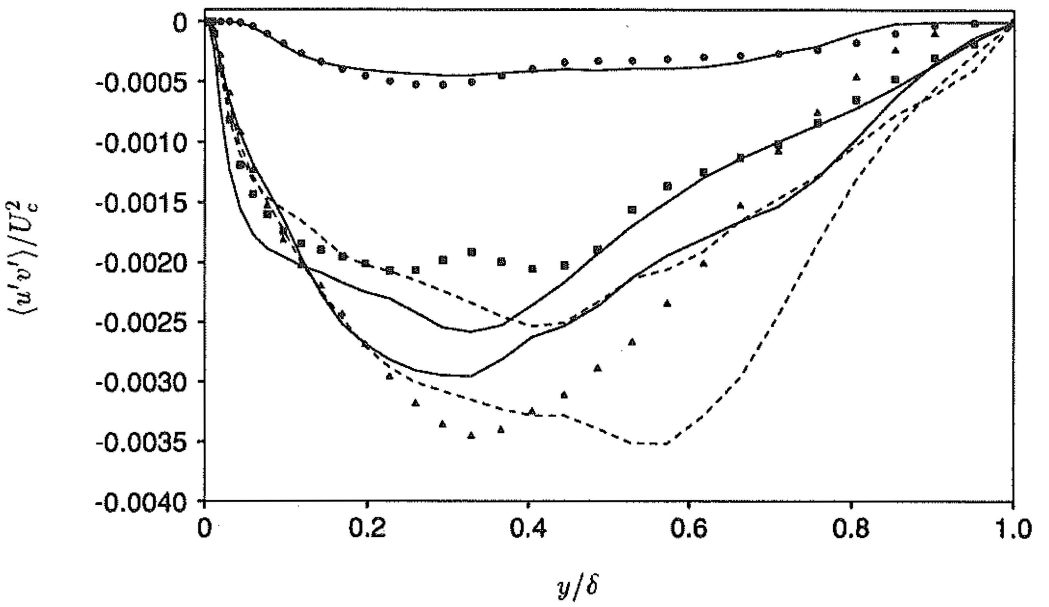

FIGURE 18. Reynolds shear stress profiles from the transitional channel flow simulation. Symbols: DNS of Zang *et al.* (1990). ● : $t = 176$; ▲ : $t = 200$; ■ : $t = 220$; ——— : Lagrangian model LES; - - - - : plane-averaged dynamic model LES.

(in units of δ). The term $\mathcal{I}_{LM}$ is initialized to 10^{-14} (instead of to zero) in order to allow the first-order Euler scheme (explicit in T^n) to move $\mathcal{I}_{LM}$ away from zero once the source term $\mathbf{L} : \mathbf{M}$ becomes non-zero.

The calculation is started on a $16 \times 65 \times 16$ mesh. As the transition process proceeds, the solution is interpolated onto increasingly finer meshes. The timings of the remeshings are determined by monitoring the energy content in the highest resolved frequencies in the streamwise and spanwise directions. The remeshing procedure was found to introduce a complication in the Lagrangian SGS model. Refining the mesh while holding the test-to-grid filter ratio fixed results in different values of $\mathbf{L} : \mathbf{M}$ and $\mathbf{M} : \mathbf{M}$. Because of its memory, the Lagrangian model requires a finite amount of time to adjust to the sudden changes in $\mathbf{L} : \mathbf{M}$ and $\mathbf{M} : \mathbf{M}$ (about $\Delta t = 5$, or 100 timesteps). In order to minimize this recovery time, the remeshing is performed with values of $\mathcal{I}_{LM}$ and $\mathcal{I}_{MM}$ rescaled so that their plane-averaged values are equal to those of the instantaneous $\mathbf{L} : \mathbf{M}$ and $\mathbf{M} : \mathbf{M}$, respectively. Early in the transition process the SGS dissipation is minuscule and errors associated with remeshing probably have a negligible effect. However, the flow may be more sensitive to remeshing at later times when the SGS dissipation is not negligible.

The $16 \times 65 \times 16$ mesh is used until $t = 145$ (in units of initial centerline velocity U_c and δ), when the grid is remeshed to $24 \times 65 \times 24$. The run is then continued to $t = 176$ on both $24 \times 65 \times 24$ and $32 \times 65 \times 32$ meshes (with little notable difference).

The field is then remeshed to $32 \times 65 \times 48$. Another remeshing to $48 \times 65 \times 64$ is performed at $t = 200$, and the simulation is then run without further remeshing to $t = 280$.

Figure 16 shows the time-history of the wall-shear stress compared with the DNS of Zang *et al.* (1990). Results from the plane-averaged dynamic model are included in this figure. The Lagrangian model is in good agreement with the DNS results up to $t = 210$. Then, the wall-shear stress slightly overshoots the peak after which it settles to a plateau, near the DNS value. The plane-averaged dynamic model results are similar, with the exception that the peak shear stress is underpredicted. Streamwise velocity fluctuations from the Lagrangian and plane-averaged models at times $t = 176$, 200, and 220 are compared with the (filtered) DNS data in Fig. 17. Overall the agreement is quite good, and at $t = 176$ it is excellent. At this time the Lagrangian and plane-averaged results are indistinguishable. Reynolds shear stresses are shown in Fig. 18. Very good agreement is obtained at $t = 176$, whereas some differences exist at $t = 200$ and $t = 220$.

Overall these results show that the Lagrangian model is capable of simulating transition. The eddy viscosity does rise from zero with a delay which is small enough so that turbulence is sufficiently damped after the rapid growth of kinetic energy during transition.

4. Summary and conclusions

A new version of the dynamic model has been tested in conjunction with the Smagorinsky closure. The model involves averaging the Germano identity for some time along fluid pathlines rather than over directions of statistical homogeneity, as was the practice in previous applications of the dynamic model. The present model is not restricted to flows with such special directions and should be readily applicable to complex-geometry, unsteady flows. We have shown that if an exponential memory is employed, the required averages can be obtained by solving a pair of relaxation-transport equations. In order to allow for the implementation of this model with minimal computational complications, we proposed to discretize the total derivatives that enter in these equations using a first-order expression in time, coupled with linear spatial interpolation to find the values required at the 'upstream' locations. The resulting formulation (embodied in Eqs. (17) and (18)) is very simple to implement.

Basic properties of the model were studied in DNS and LES of forced isotropic turbulence. The effect of the Lagrangian averaging on the pdfs of various quantities involved in the modeling were identified. It was also shown that the model preserves enough spatial locality to be influenced by vortical structures ('fat worms') that were identified in the LES.

Applications of LES to isotropic turbulence and fully developed and transitional channel flow has shown that the model performs well and should be readily applicable to more complex flows.

On a final note, we recognize that the Lagrangian dynamic model contains some arbitrary elements. In particular, an adjustable memory time scale T is involved.

This fact is unfortunate since it appears to conflict with the dynamic model philosophy of dispensing with adjustable parameters in favor of determining the subgrid-scale stress solely from information contained in the resolved velocity field. However, for any implementation which uses averaging, there is a similar ambiguity in choosing the domain over which Germano's identity is to be enforced. Schemes that make use of spatial averaging often average over all homogeneous directions although a smaller subspace may be sufficient to insure the stability of the model. Choosing a particular value of the averaging time scale in the Lagrangian model is analogous to choosing a particular region in space over which to average. When viewed in this way, the Lagrangian model actually has an advantage over spatially-averaged variants in that it is designed to average over the minimum time necessary to insure stability. This feature allows the model to retain the maximum amount of spatial and temporal variability while remaining stable.

Acknowledgements

The authors have benefited from fruitful discussions with Profs. P. Moin, J. Jimenez, and Dr. S. Ghosal. Most of this work was performed at CTR during the 1994 Summer Program. C.M. thankfully acknowledges this support from CTR, and partial support from ONR (grant N-00014-92-J-1109). T.S.L. acknowledges partial support from the ONR (grant N-00014-91-J-4072) and from the AFOSR (grant F49620-92-J0003).

REFERENCES

AKSELVOLL, K. & MOIN, P. 1993 Application of the dynamic localization model to large-eddy simulation of turbulent flow over a backward-facing step. In *Engineering applications to large-eddy simulation*, Edited by U. Piomelli and S. Ragab, ASME, New York, NY. 1–6.

BRISCOLINI, M. & SANTANGELO, P. 1994 The non-Gaussian statistics of the velocity field in low-resolution large-eddy simulation of homogeneous turbulence. *J. Fluid Mech.* **270**, 199–217.

COMTE-BELLOT, G. & CORRSIN, S. 1971 Simple Eulerian time correlation in full and narrow band velocity signals in grid generated, isotropic turbulence. *J. Fluid Mech.* **48**, 273–337.

GERMANO, M., PIOMELLI, U., MOIN, P., & CABOT, W. H. 1991 A dynamic subgrid-scale eddy viscosity model. *Phys. Fluids A.* **3**, 1760–1765.

GHOSAL, S., LUND, T. S., MOIN, P., & AKSELVOLL, K. 1994 A dynamic localization model for large-eddy simulation of turbulent flow. To appear in *J. Fluid Mech.*

JIMENEZ, J., WRAY, A. A., SAFFMAN, P.G. & ROGALLO, R. S. 1993 The structure of intense vorticity in isotropic turbulence. *J. Fluid Mech.* **255**, 65–90.

HUSSAIN, A. K. M. F., & REYNOLDS, W. C. 1970 The mechanics of a perturbation wave in turbulent shear flow. Stanford Univ. Dept. of Mech. Eng. Rep. FM-6.

KIM, J., MOIN, P., & MOSER, R. 1987 Turbulence statistics in fully developed channel flow at low Reynolds number. *J. Fluid Mech.* **177**, 133–166.

LILLY, D. K. 1992 A proposed modification of the Germano subgrid-scale closure method. *Phys. Fluids A.* **4**, 633–635.

LIU, S., MENEVEAU, C. & KATZ, J. 1994 Experimental study of similarity SGS models of turbulence in the far-field of a jet. in: *Direct and Large-Eddy Simulation of Turbulence* (eds: Voke, P., Kleiser, L., & Chollet, J. P.) , Kluwer Acad. Amsterdam. 37–49.

LUND, T. S., GHOSAL, S & MOIN, P. 1993 Numerical Experiments with highly-variable eddy viscosity models. In *Engineering applications to large-eddy simulation,* Edited by U. Piomelli and S. Ragab, ASME, New York, NY, 7–11.

MENEVEAU, C. & LUND, T. S. 1994 On the Lagrangian nature of the turbulence energy cascade. *Phys. Fluids.* **6**, 2820–2825.

O'NEIL, J. & MENEVEAU, C. 1993 On probability densities of turbulence subgrid-scale stresses and on local dynamic models (submitted to Phys. Fluids).

PIOMELLI, U. 1993 High Reynolds number calculations using the dynamic subgrid-scale stress model. *Phys. Fluids A.* **5**, 1484–1490.

PIOMELLI, U., & ZANG, T. A. 1991 Large-eddy simulation of transitional channel flow. *Comp. Phys. Comm.* **65**, 224

ROGALLO, R. 1981 Numerical experiments in homogeneous turbulence. *NASA TM 81315.*

SCOTTI, A., MENEVEAU, C. & LILLY, D. K. 1993 Generalized Smagorinsky model for anisotropic grids. *Phys. Fluids A.* **5**, 2306–2308.

VINCENT, A. & MENEGUZZI, M. 1991 The spatial structure and statistical properties of homogeneous turbulence. *J. Fluid Mech.* **225**, 1–20.

ZANG, T. A., GILBERT, N., & KLEISER, L. 1990 Direct numerical simulation of the transitional zone. In *Instability and Transition*, M. Y. Hussaini and R. G. Voigt eds., Springer-Verlag, New York, 283–299.